ADVANCED ENERGY MATERIALS
www.advenergymat.de

$NiMoO_4@Co_3O_4$ Core–Shell Nanorods: In Situ Catalyst Reconstruction toward High Efficiency Oxygen Evolution Reaction

*Getachew Solomon, Anton Landström, Raffaello Mazzaro, Matteo Jugovac, Paolo Moras, Elti Cattaruzza, Vittorio Morandi, Isabella Concina, and Alberto Vomiero**

The sluggish kinetics of the oxygen evolution reaction (OER) is the bottleneck for the practical exploitation of water splitting. Here, the potential of a core–shell structure of hydrous $NiMoO_4$ microrods conformally covered by Co_3O_4 nanoparticles via atomic layer depositions is demonstrated. In situ Raman and synchrotron-based photoemission spectroscopy analysis confirms the leaching out of Mo facilitates the catalyst reconstruction, and it is one of the centers of active sites responsible for higher catalytic activity. Post OER characterization indicates that the leaching of Mo from the crystal structure, induces the surface of the catalyst to become porous and rougher, hence facilitating the penetration of the electrolyte. The presence of Co_3O_4 improves the onset potential of the hydrated catalyst due to its higher conductivity, confirmed by the shift in the Fermi level of the heterostructure. In particular $NiMoO_4@Co_3O_4$ shows a record low overpotential of 120 mV at a current density of 10 mA cm^{-2}, sustaining a remarkable performance operating at a constant current density of 10, 50, and 100 mA cm^{-2} with negligible decay. Presented outcomes can significantly contribute to the practical use of the water-splitting process, by offering a clear and in-depth understanding of the preparation of a robust and efficient catalyst for water-splitting.

1. Introduction

The technological advancement and practical use of electrolysis are limited by the very low efficiency of cheap catalysts and the very high cost of thus efficient catalysts. Developing robust catalysts that have a relatively high performance and low-cost is still challenging. During water electrolysis, both the oxygen evolution reaction and the hydrogen evolution reactions (HER) are involved, which requires an efficient catalyst to take place at a practical rate with minimum overpotential. Accessing this catalyst has been proved as one of the main difficulties in the field of water electrolysis.[1]

Transition metals and their binary oxides have been explored for OER and encouraging results with excellent electrocatalytic activity toward OER have been obtained.[1–3] Most binary metal oxides have shown an enhanced electrical conductivity due to the interactions of metal cations, which result in higher oxidation states, leading to enhanced electrochemical properties. Among them, nickel molybdate (NiMoO4) has attracted intensive research interest due to its abundant catalytic sites, high surface area, and ease of synthesis methods.[4] Especially, the core–shell structure of metal molybdates, including $NiO@NiMoO_4$,[5] $NiCo_2O_4@NiMoO_4$,[6] $CoMoS@CoMoO_4$,[7] etc., containing nickel molybdate shell and different cores have been reported with improved catalytic activity. 3D nanorods have a high specific surface area, and their hierarchical structures further enhance the surface area and the density of surface-active sites. Besides, the electron conductivity at the surface/interface enhances the electrochemical activity. Therefore, designing core–shell metal oxides with highly conductive core and stable shell architectures would be an effective strategy to synthesize highly efficient electrocatalysts for OER.

Here, we report on the properties of the core–shell structure $NiMoO_4@Co_3O_4$, which we obtained by hydrothermal synthesis of $NiMoO_4$ nanorods followed by coating with a thin layer of Co_3O_4, using atomic layer deposition (ALD). $NiMoO_4$ nanorods with a high aspect ratio provide maximum active exposed crystal facet, which improves catalytic efficiency. Besides the intimate contact between the nickel foam substrate and $NiMoO_4$, a very thin layer of nanostructured Co_3O_4 provides a synergistic effect to boost the catalytic efficiency of the core–shell structure. The

G. Solomon, A. Landström, Prof. I. Concina, Prof. A. Vomiero
Division of Materials Science
Department of Engineering Sciences and Mathematics
Luleå University of Technology
Luleå SE-971 87, Sweden
E-mail: alberto.vomiero@ltu.se, alberto.vomiero@unive.it
Dr. R. Mazzaro, Prof. V. Morandi
Istituto di Microelettronica e Microsistemi-CNR (CNR, IMM)
Via Piero Gobetti 101, Bologna 95121, Italy
Dr. M. Jugovac, Prof. P. Moras
Istituto di Struttura della Materia-CNR (ISM-CNR)
SS 14 Km 163,5, Trieste 34149, Italy
Prof. E. Cattaruzza, Prof. A. Vomiero
Department of Molecular Sciences and Nanosystems
Ca' Foscari University of Venice
Via Torino 155, Venezia Mestre 30172, Italy

The ORCID identification number(s) for the author(s) of this article can be found under https://doi.org/10.1002/aenm.202101324.

DOI: 10.1002/aenm.202101324

versatility of ALD deposition techniques for conformally covering $NiMoO_4$ nanorods is a very attractive method to produce a promising catalytic activity toward water splitting. While the Co_3O_4@ $NiMoO_4$ structure was reported using two-step hydrothermal synthesis methods,[8] with much lower catalytic performance compared to our design, to the best of our knowledge the proposed new core–shell structure has not been reported yet. Here the chemically etched nickel surface can directly react with Mo and Ni precursors, forming a strong covalent bond, which results in vertically oriented nanorods. The catalyst results a record overpotential to reach the current density of 10 mA cm^{-2}, which is the highest reported among the known OER catalysts. We ascribe these improvements due to the hydrous nature of the core $NiMoO_4$ structure that initiates the leaching out of Mo under OER conditions, possibly resulting in abundant active sites. Also, the Co_3O_4 shell further improved the efficiency due to its enhanced electrical conductivity. Generally, this work highlights the effectiveness of the conformal coating in developing very efficient nanocomposites for OER applications. To the best of our knowledge, no catalyst has such a low overpotential, outperforming most of the noble catalysts reported for OER applications.

2. Results and Discussion

2.1. Structural and Morphological Characterizations

$NiMoO_4$@ Co_3O_4 nanorods were obtained by first synthesizing $NiMoO_4$ hydrothermally, followed by ALD Co_3O_4 deposition, as described in the experimental section and schematized in **Figure 1**a. The ALD deposition process is expected to produce a uniform thin film. Around 51 nm thick Co_3O_4 is used to conformally cover the nanorods. The deposition of Co_3O_4 to form a core–shell structure is visually confirmed by the color change, switching from the typical light yellow observed in bare $NiMoO_4$, to the deep black color achieved after deposition.

The bare $NiMoO_4$ growth process, developed by optimizing the precursors and synthesis temperature as described in the experimental section, produces well-aligned vertically grown and smooth micro rods with a high aspect ratio as shown in FE-SEM images (Figure 1b). After ALD deposition of Co_3O_4, the overall core–shell structure preserves its original shape, suggesting that the applied methods are effective in forming a core–shell structure (Figure 1c and Figure S1a,b: Supporting Information). As clearly seen in the magnified FE-SEM image in Figure 1c, the presence of Co_3O_4 changes the surface aspect, due to a uniform decoration, which increases the surface roughness, resulting in a porous texture with small Co_3O_4 nanoparticles. Indeed, the porous structure is advantageous for enhancing the charge transfer efficiency and mass transport during the catalysis process. The bare $NiMoO_4$ structure consists of well-aligned microrod arrays with smooth surfaces and an average diameter of 500 nm. There is an evident increase in the thickness of microrods (up to 570 nm) due to the coating with the Co_3O_4 layer.

The XRD pattern of as-synthesized materials, including hydrous $NiMoO_4$ and $NiMoO_4$@Co_3O_4, are shown in **Figure 2**a. The strong XRD diffraction peaks 2θ = 44.4°, 51.8°, and 76.3° correspond to the (111), (200), and (220) crystalline planes of metallic nickel (substrate) indexed by PDF# 04–0850. The remaining peaks in the diffraction pattern perfectly match the diffraction pattern of nickel molybdate hexahydrate ($NiMoO_4.xH_2O$).[9] The pattern reveals the formation of $NiMoO_4.xH_2O$ referenced by PDF# 04-017-0338, a triclinic (Anorthic) crystal structure in agreement with previously published results.[9] After coating with Co_3O_4 via ALD, the XRD pattern presents additional peaks at 2θ = 19.6°, 31.0°, 36.6°, 42.3°, 44.8°, and 61.5°. The peaks at 19.6°, 31.0°, 36.6°, and 44.8° are assigned to the spinel Co_3O_4,[10,11] while the peaks at 42.3° and

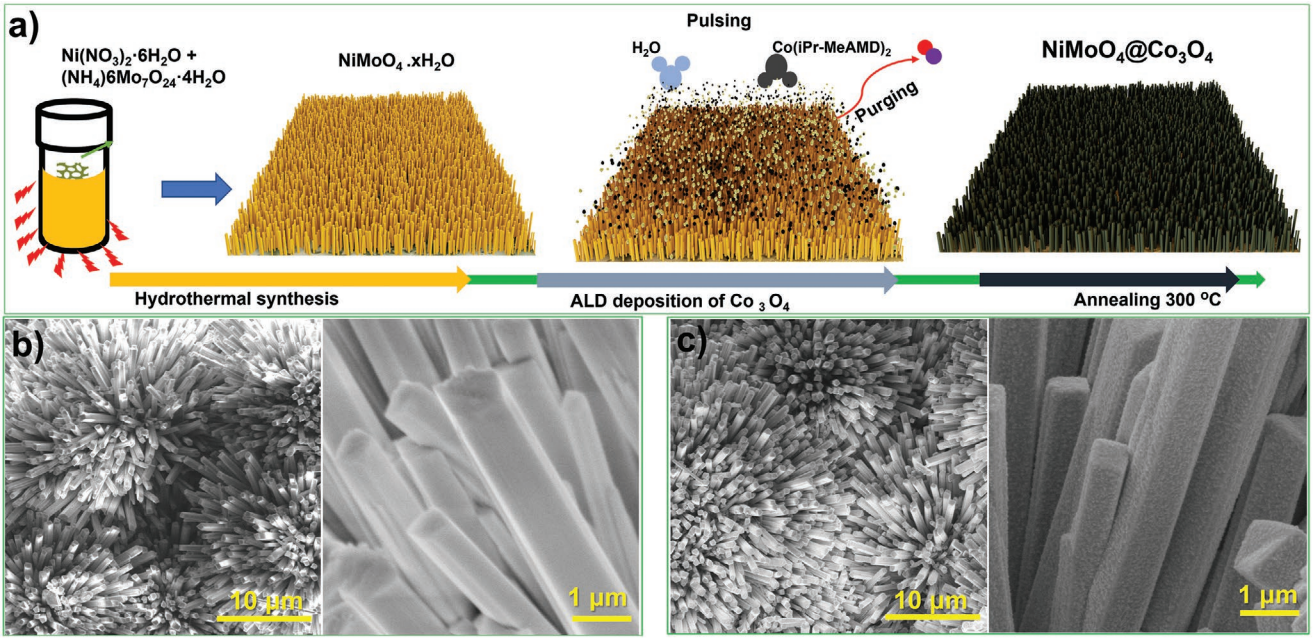

Figure 1. Schematic illustration of the synthesis methods for $NiMoO_4$ and $NiMoO_4$@Co_3O_4 a) FE-SEM images at low and high magnifications for b) $NiMoO_4$, and c) $NiMoO_4$@Co_3O_4.

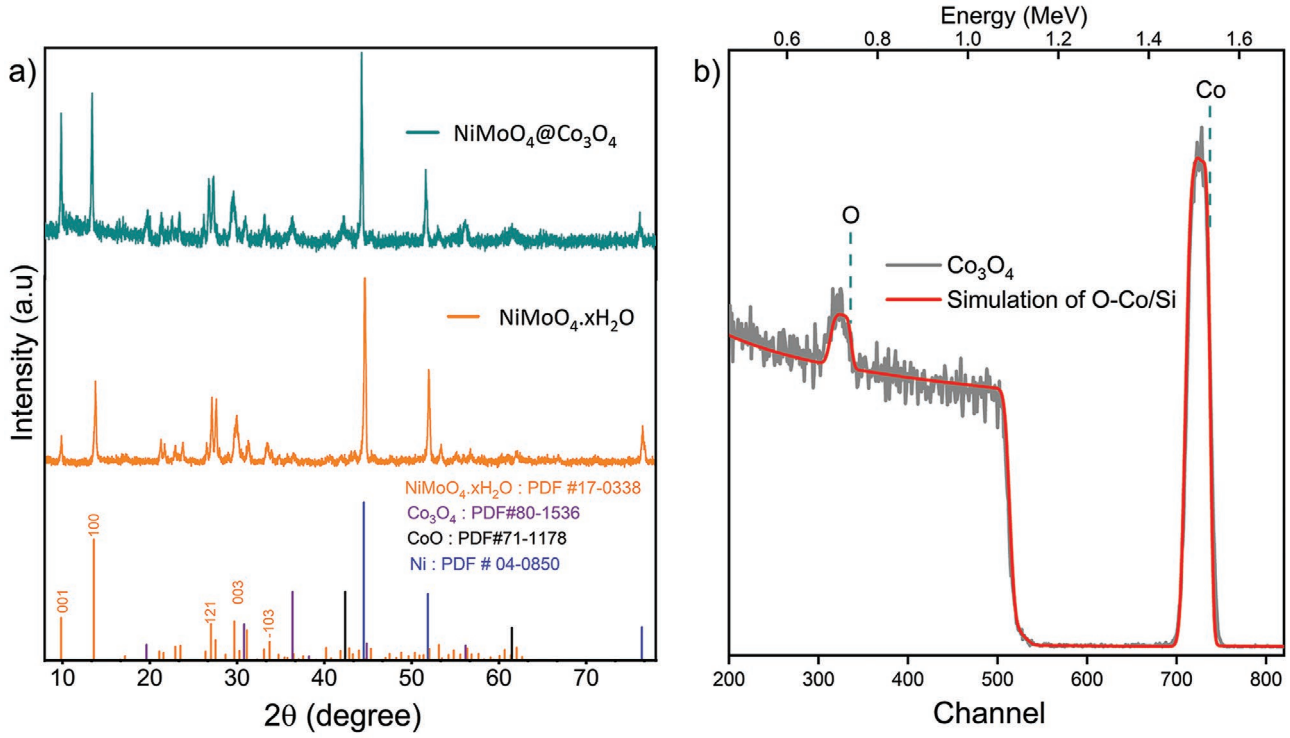

Figure 2. a) X-ray diffraction spectra of $NiMoO_4@Co_3O_4$ (cyan) and hydrated $NiMoO_4$ (yellow). Bottom line: expected reflections from hydrated $NiMoO_4$ (yellow), nickel substrate (blue), Co_3O_4 (purple), and CoO (black). b) RBS spectrum of Co_3O_4 (grey) with corresponding X-RUMP code simulation (red). The vertical dash lines indicate the surface edges for O and Co.

61.5° pertain to the (200) and (220) planes of rock-salt CoO.[11] Due to the low-temperature deposition (150 °C followed by annealing to 300 °C), the as-prepared film contains CoO phases, in agreement with the literature.[10,12] We annealed the hydrous sample at 550 °C to see the changes in the crystal structure. The XRD spectra of the hydrous $NiMoO_4$ and annealed $NiMoO_4$ samples are reported in Figure S2 in the Supporting Information. After annealing at 550 °C, the (001) peak disappears and a shift in the XRD peaks is observed (reported in Figure S2 in the Supporting Information). The diffraction patterns are indexed by nickel molybdenum oxide (Ni (MoO_4)) with a monoclinic crystal system (PDF# 86–0361).

The chemical composition and thickness of Co_3O_4 were analyzed by Rutherford backscattering spectroscopy (RBS), as shown in Figure 2b. For RBS measurement, Co_3O_4 film was grown on silicon wafers with a similar condition as that of the $NiMoO_4@Co_3O_4$ synthesis method. RBS spectra revealed the presence of O and Co, evidenced by the increase in the yield of the high-energy signal in channel 335.6 and 737.4, respectively. No contaminations were detected, within the limit of detection of the technique. From the RUMP code simulations, the Co:O atomic ratio is calculated as 3:3.5. The average Co_3O_4 thickness deposited on $NiMoO_4@Co_3O_4$ was estimated to be (50 ± 5) nm. The stoichiometry calculated from RBS confirms that Co_3O_4 contains oxygen vacancy, which is most likely due to the low temperature annealing of the catalyst.

HR-TEM analysis is performed to further study the samples before and after cobalt oxide deposition. **Figure 3**a,c reports the low magnification micrographs for the pristine and Co_3O_4 coated samples, respectively, in which the elongated morphology of the $NiMoO_4$ microcrystals can be recognized. The cobalt oxide deposition results in a homogeneous layer of sharp-cornered nanoparticles on $NiMoO_4$ nanowires surface.

High-resolution micrographs of both samples confirm the crystalline character of both nanowires and deposited nanoparticles (Figure 3b,d). The reflection pattern for the nanoparticles is compatible with the Co_3O_4 phase, as previously indicated by XRD analysis. The crystal phase of the $NiMoO_4$ nanowires is not affected by the ALD deposition process, meaning that dehydration does not occur in this low-temperature range (Figure S3, Supporting Information). The micrographs often display a set of planes parallel to the lateral edge of the nanowire, with a d-spacing compatible either with (0,1,0) axis (6.5 Å) or (1,0,0) axis (8.9 Å). This suggests that the main grown axis is (1,0,0), being orthogonal to both sets of planes. The crystal structure of hydrous $NiMoO_4$ does not change even after cobalt addition, as evidenced by the HR-TEM micrographs analysis of composites (Figure S3, Supporting Information), both exhibiting the typical crystal lattice of the hydrous $NiMoO_4$ monoclinic phase. Energy-dispersive X-ray spectrometry (EDS) confirms the presence of Ni, Mo, and Co in the heterostructures resulting from the ALD process Figures S4 and S5 (Supporting Information). The EDS mapping (Figure 3e) fully confirms the composition of both nanowires and the coating nanoparticles. Consistently, the EDS spectra profile collected along the nanowire short axis displays a spike of Co-related signal on the higher contrast nanoparticle (Figure S5, Supporting Information), as expected for the Co_3O_4 phase.

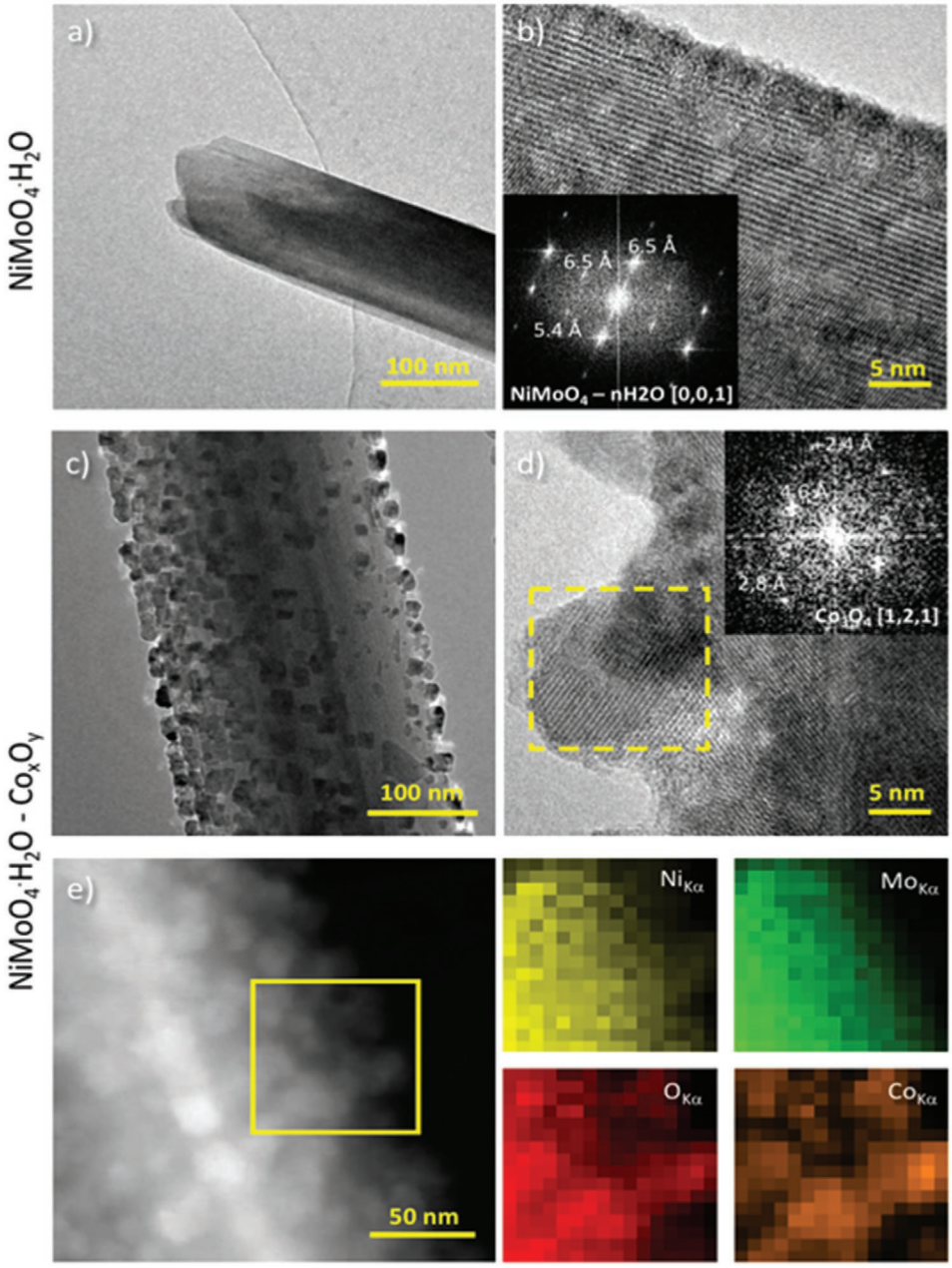

Figure 3. a,b) Low and high magnification HR-TEM micrographs for the $NiMoO_4$ sample with FFT in the inset relative to nanowire crystal pattern. c,d) Low and high magnification HR-TEM micrographs for Co_3O_4-coated $NiMoO_4$ sample with FFT in the inset relative to nanoparticle crystal pattern. e) STEM-HAADF micrograph of a Co_3O_4-coated $NiMoO_4$ nanowire and relative distribution of EDS Ka peaks for Ni, Mo, O, and Co, displaying homogenous distribution for Ni and Mo, while Co content is localized on the coating nanoparticles.

Figure 4a shows the Fourier-transform infrared spectroscopy (FTIR) spectra of the hydrated $NiMoO_4$ and NiMoO4@Co_3O_4. The broad peak around 3500 cm^{-1} (circled by blue color) is associated with the O–H stretching vibration of a hydrogen-bonded water molecule, confirming that the crystal structure contains water molecules. The δH_2O vibration is also observed at 1630.3 cm^{-1} for both samples. The FTIR peaks at 557.6 and 656.4 cm^{-1} are typically correlated with the presence of Co_3O_4 in the $NiMoO_4$@Co_3O_4 sample. The former peak is due to the stretching vibrations of the Co^{3+}– O bond and the latter is due to the bridging vibration of the Co^{2+}– O bond, respectively, as confirmed by similar works.[13–15] Interestingly, the two peaks disappear when Co_3O_4 is heat-treated above 500 °C.[16] The FTIR band around 735.3 cm^{-1} is due to the symmetric stretch of the bond Mo-Ni-O. The remaining intense peaks at 964 and 881 cm^{-1} are associated with Mo = O (symmetric and antisymmetric stretching). The FTIR peak positions agree with similar results published in the literature.[9,17,18] The annealed $NiMoO_4$ displays different FTIR spectra (Figure S6, Supporting Information) compared to the hydrous sample. As clearly seen in the

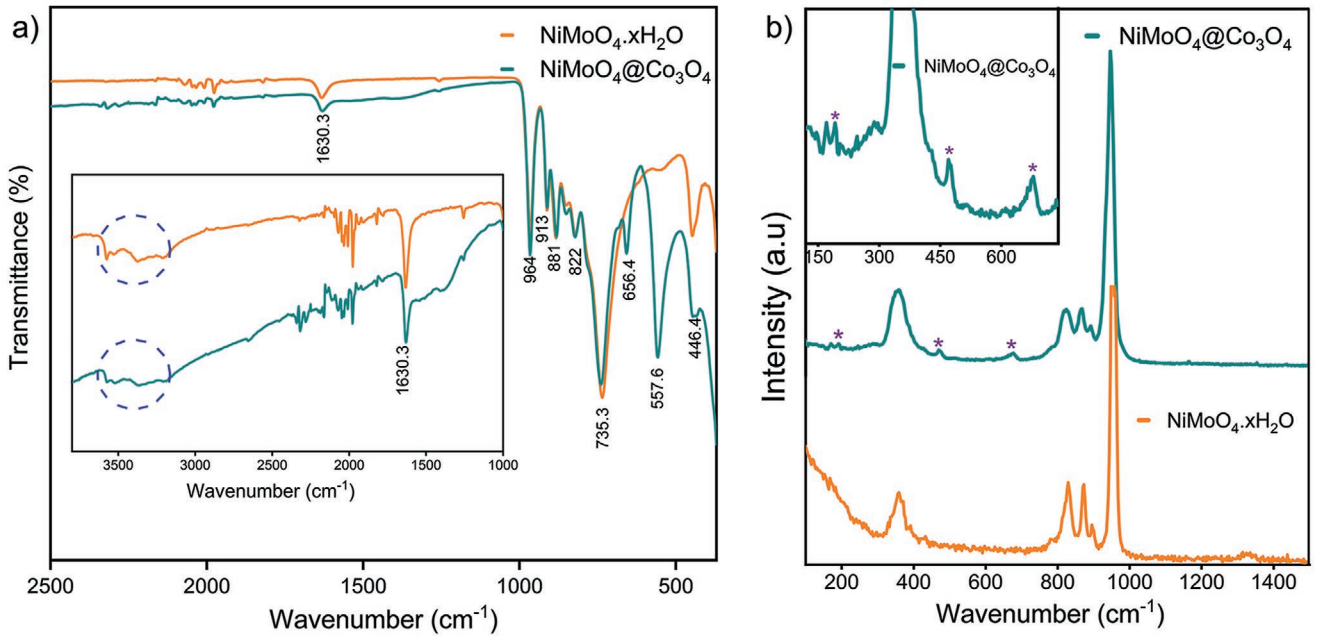

Figure 4. a) FTIR spectra of $NiMoO_4$ (yellow) and $NiMoO_4@Co_3O_4$ (green) with the inset showing the magnified spectra. b) Raman spectra of $NiMoO_4$ (yellow) and $NiMoO_4@Co_3O_4$ (green). The inset shows the resolution of the Raman peak of Co_3O_4

spectra, the peaks observed due to the O–H stretching vibration and δH_2O vibration disappear, confirming that the as-prepared sample has a hydrous crystal structure.

The Raman spectra of hydrous $NiMoO_4$ and $NiMoO_4@Co_3O_4$ (Figure 4b) display intense peaks at 948, 870, and 830 cm^{-1}, with a broad peak at 358 cm^{-1}. The Raman band located at 948 cm^{-1} for both samples is correlated with the symmetric stretching mode of molybdenum and oxygen linkage. The bands at 870 cm^{-1} are assigned to the asymmetric stretching modes of the oxygen in the O-Mo-O bond. Most of the Raman peaks observed for the hydrous samples are consistent with those reported in the literature.[9,17–19] The annealed $NiMoO_4$ samples (Figure S7, Supporting Information) show a similar Raman response, but red-shifted compared to the hydrous sample. The peaks at 959.5 and 911.5 cm^{-1} corresponds to the symmetric stretching modes of Mo–O bonds, while the peaks at 707 and 385.5 cm^{-1} are due to the asymmetric stretching mode of Ni–O–Mo bonds and the bending mode of Mo–O, respectively[20] (see Figure S7, Supporting Information). Co_3O_4 displays Raman signal at 193, 476, and 674 cm^{-1} (labeled by *). The peak positions are in agreement with the expected structure of Co_3O_4, associated with F_{2g}, E_g, F_{2g}, and A_{1g} vibrational modes of spinel-type Co_3O_4.[21,22]

2.2. Electrochemical Characterizations

Linear sweep voltammetry (LSV), chronoamperometry (I vs t), cyclic voltammetry (CV), and impedance spectroscopy measurements are conducted under 1 M KOH electrolyte using a three-electrode system configuration to reveal the electrocatalytic properties of the as-synthesized materials. As shown in **Figure 5**a the LSV for $NiMoO_4@Co_3O_4$, hydrous $NiMoO_4$, and bare nickel foam (NF) are measured using a 10 mV s^{-1} scan rate. $NiMoO_4@Co_3O_4$ shows a remarkable catalytic activity toward OER with an overpotential of 120 mV at a current density of 10 mA cm^{-2}. The substantial increase of the LSV after the onset potential is a piece of evidence for having a very high catalytic activity of the OER process. Hydrous $NiMoO_4$ possesses an overpotential of 220 mV at a current density of 10 mA cm^{-2}. The OER activity of $NiMoO_4@Co_3O_4$ is promising and exceeds the activity of the most efficient catalysts recently published (Ni–Fe oxy hydroxide@NiFe,[23] Ni-Fe oxyhydroxide,[24] NiMoOx/NiMoS[25] in terms of onset potential, and overpotential needed to produce a current density of 10 mA cm^{-2}.

To gain further insight into the OER kinetics, the Tafel slopes (after manual iR-corrections) are analyzed. As shown in Figure 5b, a Tafel slope of 58 and 78 mV dec^{-1} are obtained for $NiMoO_4@Co_3O_4$ and hydrous $NiMoO_4$, respectively. $NiMoO_4@Co_3O_4$ results in a lower Tafel slope, suggesting its highest catalytic activity compared to the hydrous $NiMoO_4$. In other words, the decrease of the Tafel slope suggested the existence of interim steps between the formation adsorbate and the rate-determining step.[26] The improved performance of the core–shell structure is evidenced by its higher catalytic current density observed in the LSV and by its lower Tafel slope (58 mV dec^{-1}). The overpotential for the three catalysts was calculated at different current densities (Figure 5c). $NiMoO_4@Co_3O_4$ retains its highest catalytic activity at different current densities (10, 50 100, and 200 mA cm^{-2}) showing an overpotential of 120, 200, 282, and 430 mV, respectively. To produce a similar current density, the hydrous bare $NiMoO_4$ requires 216, 294, 384, and 651 mV overpotentials. NF is also presented as a benchmark (Figure 5c).

To evaluate the electrocatalytic OER stability, a chronoamperometry test is conducted at different potential (Figure 5d at 1.35, 1.45, and 1.50 V vs RHE)) by continuously stepping the potential, which should produce a current density of 10, 50, and 100 mA cm^{-2}, respectively, according to the LSV

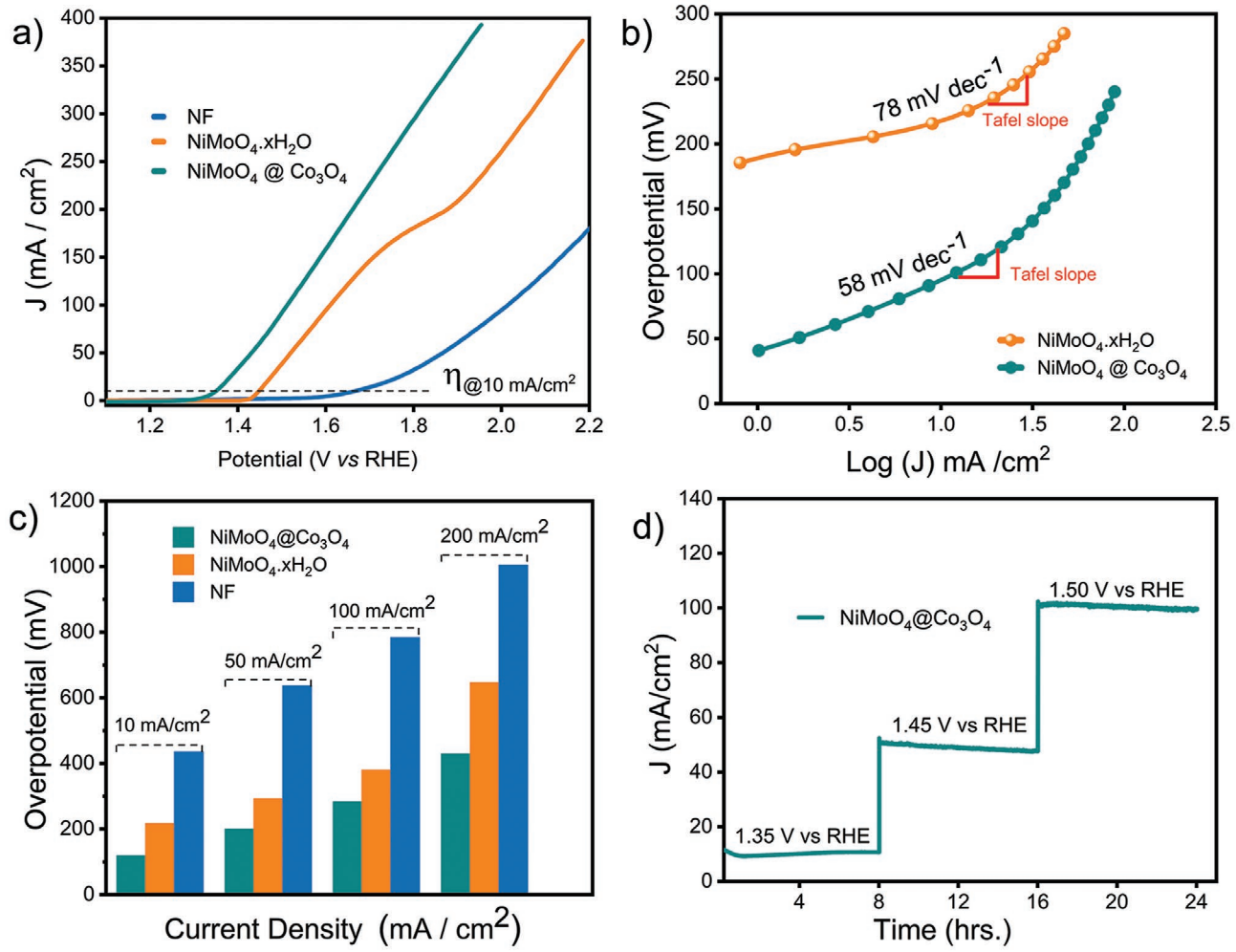

Figure 5. The OER performance of the as-prepared catalyst; a) polarization curves for $NiMoO_4@Co_3O_4$, $NiMoO_4$, and NF. b) Corresponding Tafel slope for $NiMoO_4@Co_3O_4$. c) Overpotential at different current densities, and (d) chronoamperometry (stability test) for $NiMoO_4@Co_3O_4$ at different potential associated with a current density of 10, 50, and 100 mA cm^{-2}. (LSV are provided after 5 successive scan for which the first 2 scan continuously improving the performance and last 3 scan become sable and considered here.)

measurement. Surprisingly, the stability test for $NiMoO_4@Co_3O_4$ maintains an equivalent current density observed in the LSV for consecutive 8 h operations (Figure 5d). There is no significant degradation of catalyst performance during an extended stability test (24 h). Hydrous $NiMoO_4$ also maintains the OER properties for 22 h of continuous operation at 1.50 V versus RHE (Figure S8, Supporting Information), producing ≈50 mA cm^{-2} current density, with negligible loss of performance. Both catalysts ($NiMoO_4@Co_3O_4$ and hydrous $NiMoO_4$) show remarkable stability and possess more than 98% retention of the OER current density after 8 and 22 h of continuous operation, respectively. The electrochemical surface area (ECSA) is measured using electrochemical double-layer capacitance (C_{dl}) by cycling the potential in the non-Faradaic regions (i.e., at potentials where no charge-transfer reactions occur but absorption and desorption processes can take place (**Figure 6**a,b). The $NiMoO_4@Co_3O_4$ electrocatalyst showed higher C_{dl} (2.5 mF cm^{-2}) compared to $NiMoO_4$ (0.8 mF cm^{-2}), demonstrating the higher active surface area due to the presence of Co_3O_4.

The electrochemical impedance spectroscopy (EIS) is used to understand the kinetics of the electrocatalysts at the applied potential (1.5 V vs RHE) (Figure 6d). The impedance analysis is conducted by fitting the measured spectra with simplified Randles cells as an equivalent circuit shown on the inset of Figure 6d (fitting parameters listed in Table S1: Supporting Information). The solution resistance (R_1 = 1.5 Ω) is used for iR compensation during Tafel analysis. The structure of the as-synthesized materials is very porous or not ideally smooth, hence an impedance analysis featuring constant phase elements (CPE) rather than pure capacitor is used for fitting the impedance data. $NiMoO_4@Co_3O_4$ exhibits smaller charge transfer resistance (R_{ct} = 1.1 Ω) compared to hydrous $NiMoO_4$ (R_{ct} = 2.1 Ω). The modification of Ni foam by the catalyst $NiMoO_4@Co_3O_4$ caused an improved charge transfer resistance compared to unmodified Ni foam electrode (Figure S9c and Table S1: Supporting Information). The very small charge transfer resistance indicates that Nickel foam substrate are better conductor, which minimize the potential drop at the substrate. It also helps to have a strong interactions between the

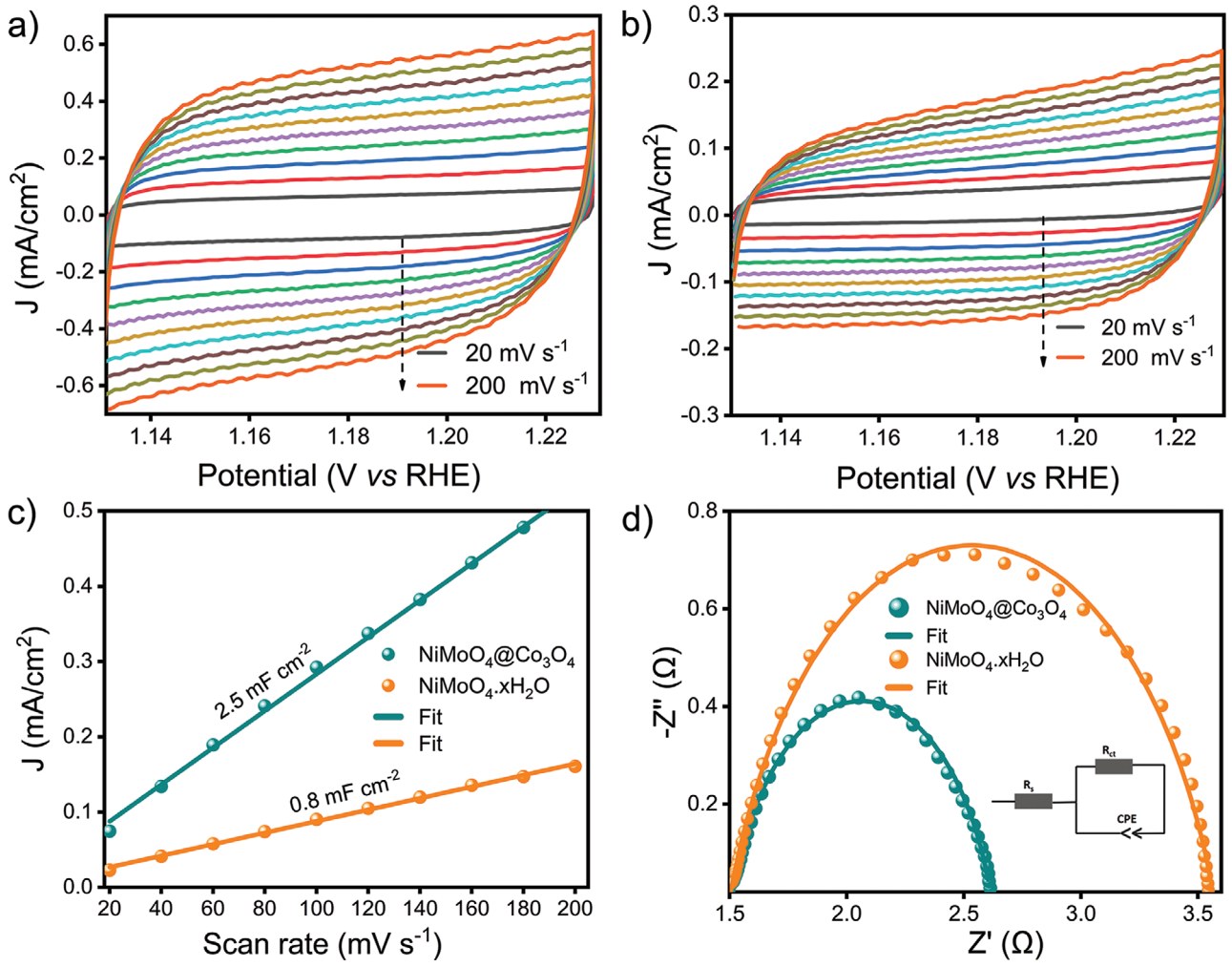

Figure 6. Cyclic voltammetry measured in the non-faradic region (1.13–1.23 V vs RHE) at different scan rates (20–200 mV^{-1}) for a) $NiMoO_4@Co_3O_4$ and b) for hydrous $NiMoO_4$. c) The difference in current density ($j = j_{anodic} - j_{cathodic}$) at 1.185 V versus RHE plotted against the scan rate and fitted to linear regression for the estimation of double-layer capacitance derived from the CV curve, and d) impedance spectroscopy of the as-prepared catalyst

catalysts and Ni substrate, producing an enhanced electrical contact, and facilitating the charge transfer, as evidenced by the smallest charge transfer resistances. The presence of Co_3O_4 leads to a more than 95% decrease of the R_{ct}, demonstrating the increase of the conductivity. Besides, for $NiMoO_4@Co_3O_4$ catalyst, an apparent exchange current density of 5.08 mA cm^{-2} is obtained and for the pristine $NiMoO_4$, a 60% lower value (3.1 mA cm^{-2}, see Equation S1 in the Supporting Information for detailed calculations).

To understand the origin of the high catalytic activity of the composites, we systematically studied by synthesizing different samples (MoO_x, NiO_x), and also by varying the annealing temperature for hydrous $NiMoO_4$. The performance (LSV) of annealed $NiMoO_4$, NF, Co_3O_4, MoO_x, NiO_x, hydrous $NiMoO_4$, and $NiMoO_4@Co_3O_4$ are measured and compared using the overpotential to produce a current density of 50 mA cm^{-2}, which is 774, 630, 573, 448, 415, 288, and 200 mV, respectively (Figure S9, Supporting Information). The EIS analysis after OER activity is displayed in Figure S9c (Supporting Information). As shown, compared to the EIS result before OER, there is a minor increase in the charge transfer resistance and higher capacitance for both hydrous $NiMoO_4$ and $NiMoO_4@Co_3O_4$. 1.6 Ω charge transfer resistance is obtained for $NiMoO_4@Co_3O_4$ after OER, compared with NF (7.48 Ω), suggesting the surface of the catalyst becoming more active and conductive (see Table S1 in the Supporting Information). Our catalyst results in a very low overpotential to reach the current density of 10 mA cm^{-2}. To the best of our knowledge, it is the highest reported among the known OER catalysts. A comparison of the catalyst with related and recently published catalysts is provided in Table S2 (Supporting Information).

During the OER process, Ni $(OH)_2$ is formed because of the reaction between Ni nanoparticles surface and OH^- ions in solution under anodic conditions. In the reverse scan Ni $(OH)_2$ can be converted into NiOOH, as a result of such redox process conditions an oxidation and reduction peak usually appeared, which are attributed to the redox couple Ni^{2+}/Ni^{3+}.[27] Such redox peak was observed in NiO_x and in MoO_x samples grown on NF substrate (Figure S9, Supporting Information), as also observed in our recent work.[26] For our catalyst, a very small peak associated

with Ni oxidation is observed for $NiMoO_4$ sample. In contrast, such peak is not observed for $NiMoO_4@Co_3O_4$ sample. However, in the reverse scan (Figure S9b, Supporting Information), the reduction of $Ni(OH)_2$ to NiOOH is observed. This could be due to the fact that the presence of Co and Mo possibly stabilize and reduces the direct exposure of Ni nanoparticles, preventing from reacting with OH^- ions. Besides, our measurement described in LSV (Figure S9a, Supporting Information), shows Ni oxidation peak for Co_3O_4, MoOx, which is due to the substrate, and Nickel foam. Especially when substrate nickel foam is not completely covered by the catalyst, the peroxidation peak is significant. However, we do not observe a redox peak because the grown film is thicker, protecting the substrate Ni from a direct contact with the solution. This phenomenon is also observed in several related works.[28–31] For the case of Co_3O_4, we could not see any redox reaction peak related to any Co^{2+}/Co^{3+} and Co^{3+}/Co^4 redox couple (Figure S9a, Supporting Information), consistent with related works.[32–34]

Hydrous $NiMoO_4$ contains two types of water molecules: surface water and coordinated water.[9] The surface water, including some portion of lattice water, should be removed when the annealing temperature is above 100 °C. In our sample, the coordination water molecules are stable even after annealing the sample up to 300 °C. Also, annealing at 300 °C does not change the performance of the catalyst toward OER. However, samples annealed at 550 °C result in very poor performance (see LSV for annealed $NiMoO_4$, Figure S8: Supporting Information). From the XRD, FTIR, and Raman analysis, we confirm that the hydrous sample can be transformed into pure crystalline $NiMoO_4$ by annealing at high temperatures (refer to Figures S2 and S7: Supporting Information). The high-temperature annealing causes a significant decrease in the current density due to the excess oxygen content, which decreases the surface defects (active sites) responsible for improving catalytic activities (in agreement with catalyst annealed at high temperature[35,36]). Other oxides such as Ru_2O,[37] Co_3O_4, and Mn_2O_3[38] also exhibit a decrease in catalytic activity with increasing temperature, which is due to the excess oxygen.[38] As a result, we ascribed the very high catalytic activity to the hydrous nature of the core $NiMoO_4$. Based on the comparison of the onset potential of the hydrous $NiMoO_4$ and $NiMoO_4@Co_3O_4$ sample (Figure 5a), the presence of Co_3O_4 also improves the onset potential of the core–shell structure. When Co_3O_4 is added to the heterostructure, a similar phenomenon of decreasing the overpotential is reported.[39] Hydrous $NiMoO_4$ helps in strengthening the electrochemical performances due to its high concentrations of active surface sites, and defective or "cracked" morphology, while cobalt decreases the overpotential due to the increase of the electrical conductivity (lower R_{ct}), which will be confirmed by the valence band measurement later. As a result, the overall performance improvement is associated with the synergistic effect of both hydrous $NiMoO_4$ and Co_3O_4 electrocatalysts.

To reveal the possible origins of the highest OER catalytic activity, the morphology, crystal structure, surface chemical states, and composition of the electrocatalyst before and after OER tests were studied. X-ray photoelectron spectroscopy (XPS) analysis was used to investigate the chemical states of the elements on the samples' surface. The core-level spectra of Mo 3d, Ni 3p, Co 3p, O 1s, C 1s, and the valence band for all samples were measured by using synchrotron radiation at VUV-Photoemission beamline, Elettra, Trieste, Italy). Additionally, the deeper Ni 2p and Co 2p core level lines were recorded by using an XPS source. **Figure 7** shows the XPS data with fitting for all samples prepared on the nickel foam substrate. The Mo 3d core level reveals that the $3d_{5/2}$ and $3d_{3/2}$ components in hydrous $NiMoO_4$ are found at 232.30 and 235.45 eV, respectively (Figure 7a). The binding energy peaks of Mo 3d are separated by 3.15 eV, thus confirming that molybdenum is in the Mo^{6+} oxidation state. These values are associated with the presence of Mo^{6+} in $NiMoO_4$.[40,41] The Mo 3d core level for $NiMoO_4@Co_3O_4$ falls at 232.28 and 235.42 eV, respectively (Figure 7a). The Ni 3p spectrum (Figure 7b) shows the main feature at lower BE, which is correlated to Ni^{2+} (Ni $3p_{3/2}$ = 67.83 eV, Ni $3p_{1/2}$ = 69.49 eV) of hydrous $NiMoO_4$ and Ni^{2+} (Ni $3p_{3/2}$ = 67.89 eV, Ni $3p_{1/2}$ = 69.61 eV) for $NiMoO_4@Co_3O_4$. The result suggested that the electron density around Ni atom decreases and the BE increases upon the formation of core shell structure with Co_3O_4. In contrast, the electron density increases around Mo atom due to the presence of Co evidenced by the very small BE shifts toward lower values. The other peak is a satellite feature of Ni $3p_{3/2}$ at 72.1 eV, and Ni $3p_{1/2}$ at 73.7 eV. The presence of Co_3O_4 nanoparticles on $NiMoO_4@Co_3O_4$ is evidenced by the Co3p feature, which is fitted with two doublets for Co in the 3^+ and 2^+ states (in agreement with the XRD result). The doublet falls at Co $3p_{3/2}$ = 60.4 eV, Co $3p_{1/2}$ = 61.5 eV, and the satellite doublet at Co $3p_{3/2}$ = 63.2 eV, Co $3p_{1/2}$ = 64.3 eV (Figure 7b), both with spin-orbit splitting of 1.1 eV.[42] For reference, we measured the Co $3p_{3/2}$ level of metallic Co at 58.44 eV.

Additional information was obtained by investigating the chemical state with an XPS lab, with an instrument capable of investigating more deeply the sample composition due to the increased electron mean free path. A quantitative analysis (related to the first 5–10 nm from the sample surface) was determined. In the hydrous $NiMoO_4$ sample, 13% C; 61% O; 10% Ni; 16% Mo composition were obtained. In the $NiMoO_4@Co_3O_4$ sample with the presence of Co, the composition shows a 15% C; 48% O; 3% Ni; 2% Mo; 32% Co; the higher amount of cobalt is detected on the $NiMoO_4@Co_3O_4$ core–shell structure due to the higher thickness of shell which cover up other two transition metals. A certain amount of carbon contamination is detected in all samples. The energy of the C 1s peak related to C—C bonds is used as a reference for the energy scale of the XPS spectra.

Ni 2p core level shows in both samples the characteristic complex shape of oxidized nickel, with the main doublet and the composite satellite structure. The position of the lower BE component (Ni $2p_{3/2}$) is centered at 855.8 and 856.0 eV in hydrous $NiMoO_4$ and $NiMoO_4@Co_3O_4$ samples, respectively, with a spin-orbit splitting of 17.5 eV (Figure S10a,b: Supporting Information): the BE values are characteristics of 2^+ state.[42,43] Moreover, the whole peak shape suggests the presence of Ni hydroxides,[44] in agreement with XRD and FTIR results. On the $NiMoO_4@Co_3O_4$ sample, the Co 2p doublet is characterized by the Co $2p_{3/2}$ signal at 780.3 eV, with a spin-orbit splitting of 15.0 eV, Figure S11 (Supporting Information), which is characteristic of cobalt oxide.[45] Its satellite shape suggests mainly the presence of Co_3O_4 compound, excluding a significant amount of both CoO and Co hydroxides.[23,45,46] The O1s core level resulted

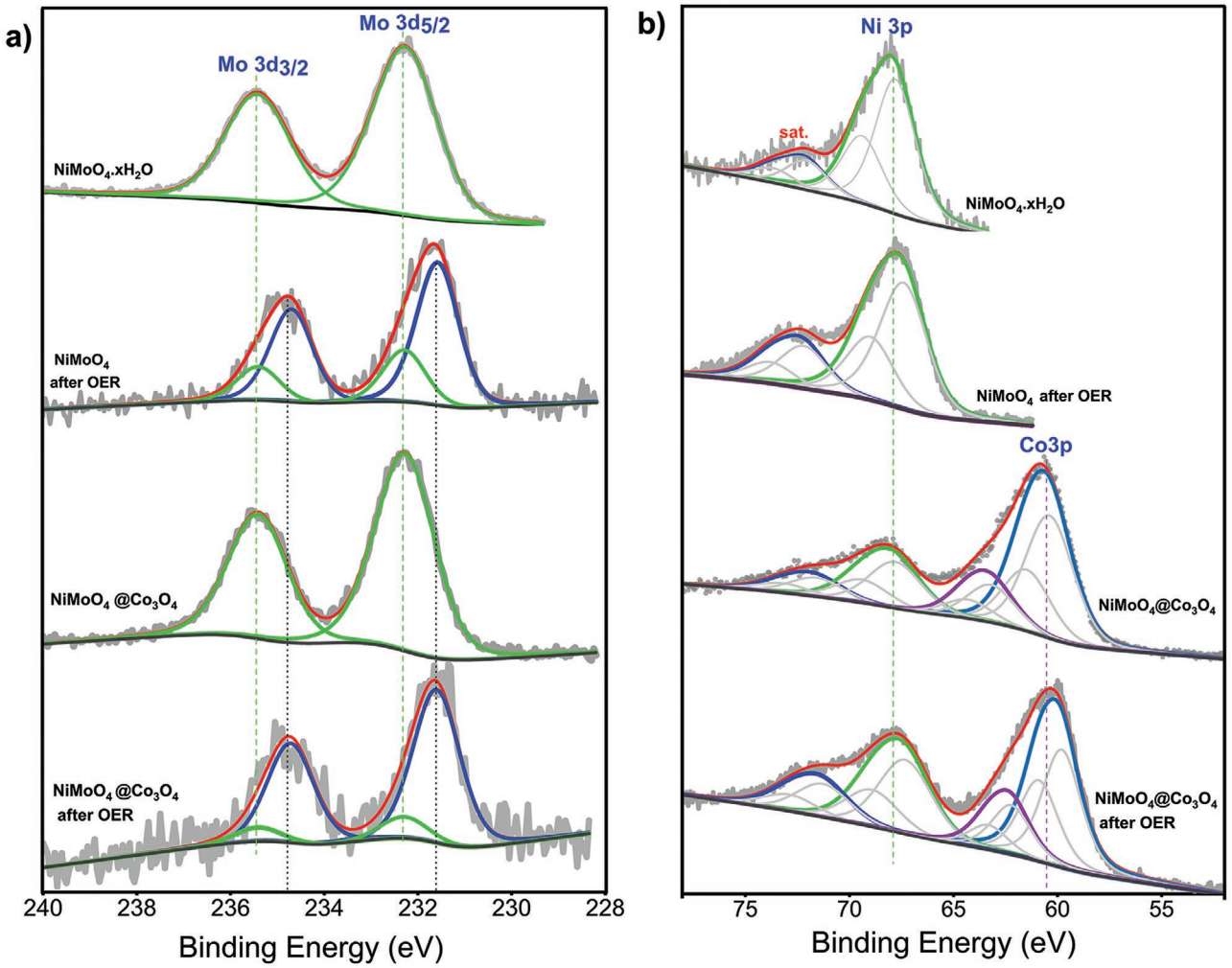

Figure 7. XPS spectra of the as-prepared catalysts. a) Mo 3d spectra for hydrous $NiMoO_4$ before and after catalysis, and Mo 3d spectra of $NiMoO_4$@Co_3O_4 before and after catalysis. b) Ni 3p spectra for $NiMoO_4$ before and after catalysis, and Ni 3p and Co 3p spectra for $NiMoO_4$@Co_3O_4 before and after catalysis. All the spectra were acquired using 690 eV p-polarized photons.

in a very broad peak in both samples, due to the multiple possible components related to the chemical bond of oxygen with both Ni and Mo, as well as with (a limited amount of) C. Under the rough hypothesis for every Mo atom, there are 3 O atoms involved in chemical bonds, for every Ni atom, there are 1 O atoms involved, and for every Co atom there are 1.3 O atoms involved, then the quantitative analysis from XPS (reported before) is consistent with the chemical bond attribution.

Post OER characterization of hydrous $NiMoO_4$ and $NiMoO_4$@Co_3O_4 samples showed a lower BE of Mo, Ni, and Co peaks (refer to Figure 7). The BE of the $Mo3d_{5/2}$ component changed to 231.7 eV (0.6 eV decrease). This value indicates a possible variation of the Mo oxidation state toward 5+ (Mo becoming more metallic).[40] The main and satellite peaks of Ni for both samples after OER tests also shift toward lower binding energy (of about 0.4 eV). Also, Co levels tend to shift to lower BE (of about 0.6 eV). The hydrous $NiMoO_4$ sample after OER showed 6% C, 60% O, 27% Ni, 1% Mo, and 6% K composition: the main difference after OER is the appearance of a large amount of Ni and a strong decrease of Mo in the first few nm from the sample surface. Here, the Ni 2p peak position falls at BE slightly lower than before OER (around 0.4 eV); the band shape suggests the presence of a large amount of Ni hydroxide.[44] The $NiMoO_4$@Co_3O_4 sample after OER exhibited the following composition: 12% C, 49% O, 13% Ni, 1% Mo, 22% Co, and 3% K, then showing in the measured region a marked increase of Ni and a decrease of Mo as a consequence of OER tests. Here too, the Ni 2p peaks shifted toward lower BE after OER (about 0.5 eV), with a band shape suggesting the presence of an increased amount of Ni hydroxides. In this sample, also the Co 2p related peaks slightly shift toward lower BE after OER (of about 0.2 eV) but with the same band shape as before OER, thus confirming the presence of Co_3O_4 compound and excluding a significant amount of both CoO and Co hydroxides.[45] After OER a shift in the BE to lower values are observed for Mo, Ni and Co atom XPS peak. In several works, an increase in oxidation state is observed after catalysis, due the further oxidation of the metal catalyst on the surface by the anodic potential. However, for our cases a lower BE is observed after OER test. In fact, this phenomenon is also confirmed by the absence

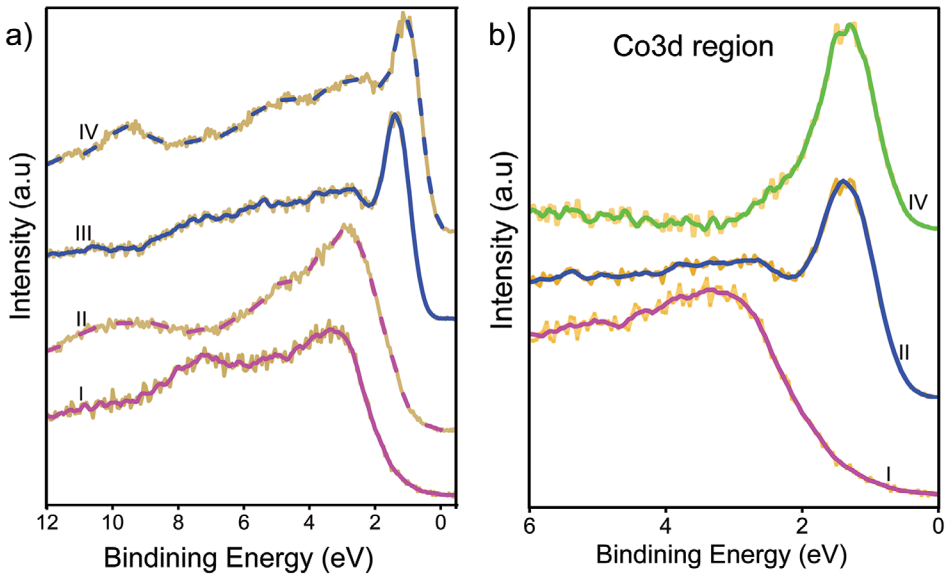

Figure 8. a) Valence band spectra for hydrous $NiMoO_4$ (I), $NiMoO_4$ after OER test (II), $NiMoO_4@Co_3O_4$ (III), and $NiMoO_4@Co_3O_4$ after OER test (IV). b) The green spectrum (IV) is obtained as a difference between the blue (II) and the pink spectra (I).

of oxidation peak during the LSV measurement (Figure 5a) for $NiMoO_4@Co_3O_4$. Therefore, we conclude that the metal cation (Ni, MO, and Co) participates on the electron transfer process on the interface during the OER process.

These experimental findings are in agreement with data acquired using synchrotron radiation: also the additional bands detected by the X-ray source (Ni 2p and Co 2p) were characterized by BE lower than before OER tests, suggesting a slightly more metallic behavior of Ni and Co, but also evidencing a marked amount of Ni hydroxides after OER test. The result indicates that the catalyst reconstructs into other phases during the catalysis process, which maintains the performance of the catalyst (further examined using in situ Raman spectroscopy).

The use of synchrotron radiation helps to investigate the valence band of the samples (**Figure 8**). The valence spectrum of $NiMoO_4$ explained the origin of its insulating behavior, normally due to the strong hydration effect associated with crystalline water. The first peak below the Fermi level is seen at about 3.6 eV. $NiMoO_4$ has a direct gap of 2.3 eV and an indirect gap of 1.9 eV.[47] By extrapolating the linear part of the $NiMoO_4$ spectrum toward low BE, we determine the valence band position maximum, which is located at 1.2–1.6 eV below the Fermi level. $NiMoO_4$ samples after the OER test have the first peak below the Fermi level, which shifts to 3.1 eV BE and the valence band maximum rises to 1.0–1.3 eV, confirming that the catalyst becomes more conductive during the OER process. This finding is a direct evidence for crystal surface reconstruction of hydrous $NiMoO_4$ during the catalysis process. Especially, the loss of the crystalline water during the OER process could increase the conductivity of the sample, which could be the reason for the shift of valence band peaks to 3.1 eV.

The valence spectrum of $NiMoO_4@Co_3O_4$ is completely different from bare $NiMoO_4$ in the proximity of the Fermi level. A prominent feature with a maximum at 1.7 eV is seen in $NiMoO_4@Co_3O_4$ catalyst, which could be assigned to the emission from Co 3d states, as visible from the green spectrum in Figure 8b, obtained as a difference between the $NiMoO_4@Co_3O_4$ and hydrous $NiMoO_4$ valence band measurements. This peak is possibly composed of the main contribution at 1.7 eV and a smaller peak at 2.5 eV. Its shape and energy position indicates the formation of Co_3O_4 nanoparticles, confirming the presence of this compound as also suggested by the Co 2p band shape. These features are present in Co_3O_4 and absent in CoO.[48] Moreover, Co_3O_4 has an energy gap of 0.8 eV; by extrapolating the linear part of the $NiMoO_4@Co_3O_4$ spectrum, we found a valence band maximum of 0.7 eV. In the $NiMoO_4@Co_3O_4$ sample after OER, a shift of all spectroscopic features by 0.4 eV and the appearance of the peak at 10 eV is observed, similarly to sample $NiMoO_4$ after OER.

In addition, morphology characterization after OER test confirms that the nanorods structure is preserved after the long-term stability test as shown in **Figure 9**a, indicating their structural stability toward OER, suggesting that the stability of the catalyst after OER process. The EDS map sum comparison (Figures S1, S12, and S13: Supporting Information) reveals that, after the OER test, a similar uniform distribution of Ni, Co, O elements is observed but with very low Mo content. Dissolution or leaching out of Mo occurs, which results in nickel hydroxide formation. However, structural destruction of nanorods does not occur, and the morphology of the nanorod is preserved after the OER test.

The XRD pattern of the catalyst after OER illustrates the absence of most of the XRD peaks associated with Co_3O_4 reflections, except the peak at 36.3°, which is present in both (CoO and Co_3O_4) phases in situ(Figure 9b). Also, there is no peak associated with hydrous $NiMoO_4$ samples, suggesting an amorphous nature of the crystal after catalysis. However, the XRD peak of CoO remains unchanged at $2\theta = 36.3°$, 42.2°, and 61.5° (PDF# 076–3330) (Figure 9b). This suggested that the extended stability test does not affect the CoO phase, indicating

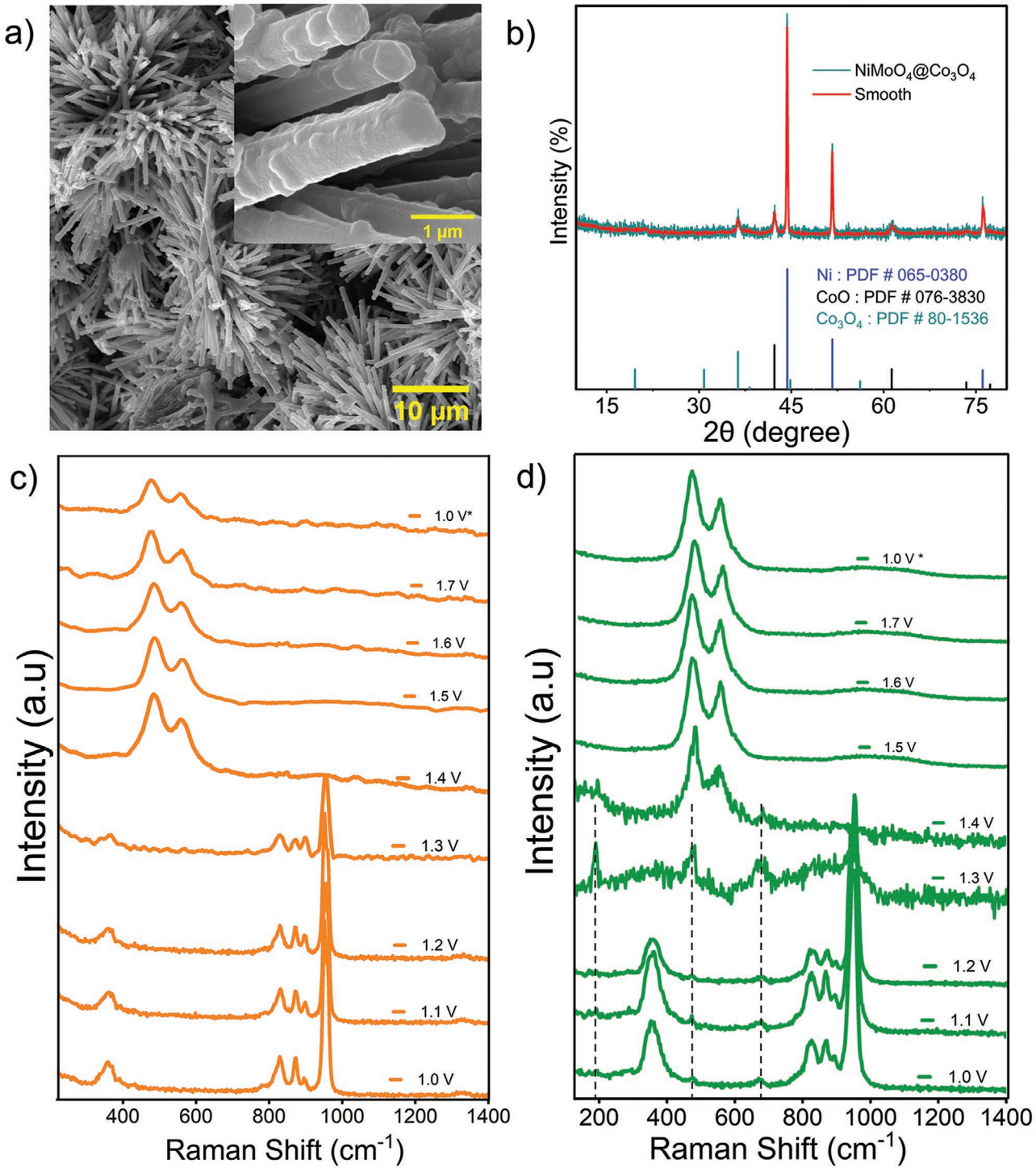

Figure 9. Post OER characterizations: a) SEM images and b) XRD pattern for $NiMoO_4@Co_3O_4$. In situ Raman characterization at different anodic potential (V) versus RHE for c) hydrated $NiMoO_4$, and d) for $NiMoO_4@Co_3O_4$

the stability of the CoO phases under the long-term stability test. Co^{3+} in Co_3O_4 shows structural transformation into CoO under alkaline conditions, and it is one of the dominant active sites in the OER reaction, as confirmed by related works.[39,49] Especially, defective Co_3O_4 with oxygen vacancy has been reported as effective in catalyzing OER.[50,51] In our catalyst, the RBS result revealed that Co_3O_4 has oxygen deficiency. As a result, the defective Co_3O_4 more easily adsorb oxygen intermediates (OH^*), which could form cobalt hydroxide and later easily released oxygen gas. During this process, Co_3O_4 undergoes surface reconstruction and amorphization (evidenced by the absence of the Co_3O_4 XRD peaks (Figure 9b) and availability

of the Co^{3+} cation detected in post OER XPS result (Figure 7). However, the very high catalytic efficiency of the composites is not affected, suggesting the process induces an in situ creation of active sites.

It is known that metal-based electrocatalysts undergo surface reconstruction during the catalysis process. Such reconstruction can be irreversible[52–54] or reversible[55,56] depending on the nature of the catalyst and reaction medium. For instance, during the OER test of CoS_x, the catalyst surface transformed irreversibly into CoOOH, a catalytically active and efficient OER catalyst.[52] In a related work,[55] CoO_xH_y modified with Ni underwent an irreversible transformation that began with spinel structure to an amorphous CoO structure at low anodic potentials. Similarly, in our work, we have conducted operando Raman measurements to study the phase changes during the catalysis process (setup and description are available in Figure S12 in the Supporting Information). Figure 9c presents the Raman signal of hydrous $NiMoO_4$ at different potentials. The in situ Raman helps monitor the newly generated phase upon the OER process. The results revealed that the nanorods undergo reconstruction during the OER process evidenced by the newly evolved Raman peak above 1.4 V versus RHE. The surface reconstruction is not reversible as confirmed by the Raman characteristics peak measured at 1.0 V versus RHE at the end of the measurement. The two well-defined Raman peaks observed around 477 and 555 cm^{-1} are characteristics of NiOOH species,[57,58] in agreement with the XPS measurements of Ni 2p core level, suggesting the presence of Ni hydroxides. We have also conducted in situ Raman characterization for the annealed $NiMoO_4$ sample (Figure S13, Supporting Information). When the anodic potential increases to 2.2 V, a different phenomenon compared to hydrous $NiMoO_4$ is observed. For this sample, the Raman bands at 959.5 and 911.5 cm^{-1}, assigned to the symmetric and asymmetric stretching modes of the Mo=O bond remain stable with the increasing anodic potential. However, for the hydrous sample, the peak associated with the Mo=O bond disappeared with increasing potential (Figure 9c). For the annealed $NiMoO_4$, the NiOOH peak starts to appear when the anodic potential increases above 1.6 V versus RHE. Also, the peak at 260 cm^{-1}, attributed to the deformation mode of Mo–O–Mo, disappeared when NiOOH peak started to exist. No significant change was observed for the peak at 707 cm^{-1}. The peak at 385.5 cm^{-1}, associated with the bending mode of Mo–O started to attenuate above 1.6 V versus RHE. This analysis confirms that the hydrous structure can easily reconstruct, and bonds related to Mo atoms are not visible anymore.

The in situ Raman characterization for $NiMoO_4@Co_3O_4$ is also displayed in Figure 9d: a similar trend is observed with increasing applied potential. The presence of Co_3O_4 does not protect the heterostructure from the reconstruction. The only difference with bare $NiMoO_4$ catalyst is that the reconstruction process starts at lower potential (around 1.3 V vs RHE), suggesting more rapid OER catalytic kinetics. Co_3O_4 displays weak Raman signal at 193, 476, and 674 cm^{-1}, however, these peaks disappear with a further increase of the applied potential. Ni-based catalyst shows progressive oxidation to nickel hydroxide before OER reaction.[55,59] However, our operando Raman characterization shows that the formation of NiOOH is observed after the OER process. This suggested that the active sites of our catalyst are not only the in situ-created hydroxide but also the as-synthesized catalyst itself. As the potential is raised above 1.2 V (Figure 9d), the peaks belonging to Co_3O_4 rapidly attenuate, and the Raman signal at 193, and 674 cm^{-1} disappear, consistent with reported literature results.[60,61] A possible conclusion cannot be drawn from the Co_3O_4 Raman peak at 467 cm^{-1} because it overlaps with the Raman peak of nickel hydroxide (Figure 9d). However, the possibility of cobalt hydroxide formation cannot be excluded. The absence of XRD peak associated with Co_3O_4, $NiMoO_4$, and NiOOH after the OER process suggested that the catalyst transformed into an amorphous phase.

Based on in situ Raman analysis and post-OER characterizations we highlight important conclusions. Hydrated $NiMoO_4$ completely reconstructed, without losing the nanorod morphology. Both the spinel Co_3O_4 and hydrated $NiMoO_4$ were not recovered after the catalysis process, rather they are completely transformed into CoO species and NiOOH, respectively. Also, an irreversible transformation into an amorphous phase containing CoO species was observed after the stability test as well as during the in situ Raman test, for anodic potential above 1.4 V versus RHE.

Reconstruction of metal hydrates under alkaline conditions is also observed and documented in different research works. For instance, $NiMoO_4$ and NiO displayed in situ oxidation to NiOOH under OER conditions.[62,63] Boon et al. observed gradual oxidation of Co_3O_4 to CoO(OH) with increasing applied potential and the oxidation improved the OER activity due to the presence of Co^{IV} cations.[60] Zhaohui et al. verified that the presence of oxygen vacancy in spinel Co_3O_4 considerably increases the formation of surface CoOOH, which enhances the OER activity.[50]

For both cases, the transformation is irreversible and observed exclusively under in situ conditions. Besides, Zhu et al. demonstrated that Ni containing spinel Co_3O_4 catalyst transformed in NiOOH-CoO species, and that the presence of Ni is vital in initiating the spinel Co_3O_4 to CoO transformation.[55] The structural conversion observed for Co_3O_4 by our in situ Raman spectroscopy is similar to the result obtained from Zhu et al. However, in our case, the transformation is not reversible for the $NiMoO_4@Co_3O_4$ catalyst. To double-check we have conducted in situ Raman characterization for Co_3O_4 (Figure S13b). Co_3O_4 shows a stable Raman signal under applied potential. The Raman peaks are stable and show a minor decrease when the potential is increased to 2 V. The Raman peak starts to minimize, and no other phases are observed. Especially the formation of bubbles and changes that occur on the surface at higher potential are the only factors that make the Raman signal disappeared temporarily. This is confirmed by the Raman signal measured by taking out the sample from in situ measurement and dried it for the last measurement. We found that the Raman peak is completely recovered (Figure S13b (Supporting Information), Top spectrum). We concluded that for $NiMoO_4@Co_3O_4$ catalyst, the transformation of Co_3O_4 into amorphous structure is initiated by the presence of Ni and Mo, which is in agreement with very few literatures results.[64–66]

The absence of the Molybdenum-related Raman band above 1.3 V versus RHE in the hydrous $NiMoO_4$ and $NiMoO_4@Co_3O_4$ catalyst confirms that Mo leaches from the crystal structure. We confirm the leaching out of Mo species by the drastic decrease

of Mo concentration in the EDS quantitative analysis performed after the stability test at the sample place (Figure S12, Supporting Information) and by scratching the powder (Figure S13, Supporting Information). In both cases, a very low Mo concentration is detected. The XPS quantitative analysis after the OER stability test also confirms a 1% Mo atom. Therefore, Mo species are leached out during the crystal reconstruction of hydrate $NiMoO_4$.The presence of Co_3O_4 does not help in preventing Mo loss. Such a trend was also observed for bimetallic NiMo nitride electrocatalyst.[67] We observed that such leaching does not affect the catalytic performance negatively, as evidenced by the long-term stability test. Indeed, the dissolution of Mo can open the structure and maximize the contact area with the electrolyte, which increases the density of surface sites. Besides, Mo vacancies are highly active toward OER activity because it enhances the OER activity by forming OH-containing intermediates which are vital for the OER process. For instance, for $NiMoO_4@Co_3O_4$ catalyst an increased Ni contents and decrease of Mo content (12% C, 49% O, 13% Ni, 1% Mo, 22% Co, and 3% K) was observed. The quantitative analysis and the in situ Raman result together suggested that the in situ created Nickel hydroxide are the dominant phase on the topmost surface of the catalyst and the Mo leaching leaves a avoids surface resulting and maximized active site responsible for the formation of OER intermediates. Generally, the hydrous sample, which is highly crystalline as a core, and the semicrystalline Co_3O_4 shell results in an efficient catalyst due to the ease of the reconstruction process of the hydrate, which results in very high actives surface site density, and thanks to the improved conductivity of the composite after the addition of Co_3O_4.

3. Conclusion

In summary, we have synthesized $NiMoO_4@Co_3O_4$ core–shell structure, which is a unique OER-active catalyst, showing a remarkable catalytic activity toward OER with a record low overpotential of 120 mV to produce a current density of 10 mA cm^{-2} and a Tafel slope of 58 mV dec^{-1}. The results prove that the presence of Co_3O_4 improves the electrical conductivity of the core–shell structure, which enhances the onset potential of the heterostructure.

Operando Raman characterization proves that hydrous $NiMoO_4$ and $NiMoO_4@Co_3O_4$ underwent irreversible surface reconstruction and produces nickel hydroxide. We showed that this catalyst reconstruction process plays an important role in maintaining the highest OER activity. The dissolution of Mo species from the nanorods leads to catalytically active surface site centers in the crystal structure, which does not negatively affect the morphology and the catalyst performance, as evidenced by the long-term stability. The presence of oxygen defects on Co_3O_4, the hydrous nature of $NiMoO_4$ which undergoes surface reconstruction, and the presence of crystalline water which facilitates the leaching out of Mo atoms are the main responsible factors for enhancing the surface abundant sites.

In general, coating the hydrous catalyst by Co_3O_4 improves the electrical conductivity and maintains its highest catalytic activity of the heterostructure toward OER. Our findings can significantly boost and advance the practical exploitation of the water-splitting process using very cheap and efficient catalysts toward hydrogen production.

Supporting Information

Supporting Information is available from the Wiley Online Library or from the author.

Acknowledgements

The authors acknowledge the financial support from Knut & Alice Wallenberg foundation, the Swedish foundation consolidator fellowship, the European Union's Horizon 2020 research and innovation program under grant agreement No 654002, Luleå University of Technology laboratory fund program, and Kempe Foundation for partial funding. I.C. acknowledges VINNOVA under the VINNMER Marie Curie incoming Grant for partial funding (project "Light Energy", LiEN, 2015-01513). The research leading to this result has been supported by the project CALIPSOplus under Grant Agreement 730872 from the EU Framework Programme for Research and Innovation HORIZON 2020 (beamtime nr. 20205170, VUV-PHotoemission beamline, Elettra, Trieste, Italy). This work has been carried out within the agreement "Convenzione operativa per collaborazione scientifica tra CNR ISM e Dipartimento di Scienze Molecolari e Nanosistemi Università Cà Foscari Venezia (Prot.n. 709, 14/04/2021)". Partial support through the project EUROFEL-ROADMAP ESFRI is gratefully acknowledged.

Conflict of Interest

The authors declare no conflict of interest.

Data Availability Statement

Research data are not shared.

Keywords

atomic layer deposition, core–shell structure, electrocatalysts, hydrous catalysts, oxygen evolution reaction, water splitting

Received: April 27, 2021
Revised: June 5, 2021
Published online: July 14, 2021

[1] Q. Hu, G. Li, Z. Han, Z. Wang, X. Huang, H. Yang, Q. Zhang, J. Liu, C. He, *J. Mater. Chem. A* **2019**, *7*, 14380.
[2] X. Peng, C. Pi, X. Zhang, S. Li, K. Huo, P. K. Chu, *Sustainable Energy Fuels* **2019**, *3*, 366.
[3] Z. Chen, X. Duan, W. Wei, S. Wang, B. J. Ni, *J. Mater. Chem. A* **2019**, *7*, 14971.
[4] F. Chen, S. Ji, Q. Liu, H. Wang, H. Liu, D. J. L. Brett, G. Wang, R. Wang, *Small* **2018**, *14*, 1800791.
[5] D. Jia, H. Gao, L. Xing, X. Chen, W. Dong, X. Huang, G. Wang, *Inorg. Chem.* **2019**, *58*, 6758.
[6] X. Du, J. Fu, X. Zhang, *ChemCatChem* **2018**, *10*, 5533.
[7] Y. R. Liu, X. Shang, W. K. Gao, B. Dong, X. Li, X. H. Li, J. C. Zhao, Y. M. Chai, Y. Q. Liu, C. G. Liu, *J. Mater. Chem. A* **2017**, *5*, 2885.
[8] X. Du, N. Li, X. Zhang, *Dalton Trans.* **2018**, *47*, 12071.

[9] K. Eda, Y. Kato, Y. Ohshiro, T. Sugitani, M. S. Whittingham, *J. Solid State Chem.* **2010**, *183*, 1334.
[10] J. X. Flores-Lasluisa, J. Quílez-Bermejo, A. C. Ramírez-Pérez, F. Huerta, D. Cazorla-Amorós, E. Morallón, *Materials* **2019**, *12*, 1302.
[11] S. Jung, D. K. Nandi, S. Yeo, H. Kim, Y. Jang, J. S. Bae, T. E. Hong, S. H. Kim, *Surf. Coat. Technol.* **2018**, *337*, 404.
[12] P. Ghamgosar, F. Rigoni, M. G. Kohan, S. You, E. A. Morales, R. Mazzaro, V. Morandi, N. Almqvist, I. Concina, A. Vomiero, *ACS Appl. Mater. Interfaces* **2019**, *11*, 23454.
[13] K. B. Klepper, O. Nilsen, H. Fjellvåg, *Thin Solid Films* **2007**, *515*, 7772.
[14] X. Shi, S. Quan, L. Yang, C. Liu, F. Shi, *J. Mater. Sci.* **2019**, *54*, 12424.
[15] S. Sahoo, A. K. Satpati, *J. Electroanal. Chem.* **2017**, *801*, 416.
[16] Y. Li, W. Qiu, F. Qin, H. Fang, V. G. Hadjiev, D. Litvinov, J. Bao, *J. Phys. Chem. C* **2016**, *120*, 4511.
[17] A. P. De Moura, L. H. De Oliveira, I. L. V. Rosa, C. S. Xavier, P. N. Lisboa-Filho, M. S. Li, F. A. La Porta, E. Longo, J. A. Varela, *Scientific World J.* **2015**, *2015*, 1.
[18] H. Wan, J. Jiang, X. Ji, L. Miao, L. Zhang, K. Xu, H. Chen, Y. Ruan, *Mater. Lett.* **2013**, *108*, 164.
[19] D. Ghosh, S. Giri, C. K. Das, *Nanoscale* **2013**, *5*, 10428.
[20] P. R. Jothi, K. Shanthi, R. R. Salunkhe, M. Pramanik, V. Malgras, S. M. Alshehri, Y. Yamauchi, *Eur. J. Inorg. Chem.* **2015**, *2015*, 3694.
[21] B. Rivas-Murias, V. Salgueiriño, *J. Raman Spectrosc.* **2017**, *48*, 837.
[22] V. G. Hadjiev, M. N. Iliev, I. v. Vergilov, *J. Phys. C: Solid State Phys.* **1988**, *21*, L199.
[23] C. Liang, P. Zou, A. Nairan, Y. Zhang, J. Liu, K. Liu, S. Hu, F. Kang, H. J. Fan, C. Yang, *Energy Environ. Sci.* **2020**, *13*, 86.
[24] M. Görlin, J. Halldin Stenlid, S. Koroidov, H. Y. Wang, M. Börner, M. Shipilin, A. Kalinko, V. Murzin, O. v. Safonova, M. Nachtegaal, A. Uheida, J. Dutta, M. Bauer, A. Nilsson, O. Diaz-Morales, *Nat. Commun.* **2020**, *11*, 6181.
[25] P. Zhai, Y. Zhang, Y. Wu, J. Gao, B. Zhang, S. Cao, Y. Zhang, Z. Li, L. Sun, J. Hou, *Nat. Commun.* **2020**, *11*, 5462.
[26] G. Solomon, M. G. Kohan, M. Vagin, F. Rigoni, R. Mazzaro, M. M. Natile, S. You, V. Morandi, I. Concina, A. Vomiero, *Nano Energy* **2021**, *81*, 105664.
[27] M. Urso, G. Torrisi, S. Boninelli, C. Bongiorno, F. Priolo, S. Mirabella, *Sci. Rep.* **2019**, *9*, 7736.
[28] C. C. Cheng, P. Y. Cheng, C. L. Huang, D. Senthil Raja, Y. J. Wu, S. Y. Lu, *Appl. Catal., B* **2021**, *286*, 119916.
[29] B. Q. Li, C. Tang, H. F. Wang, X. L. Zhu, Q. Zhang, *Sci. Adv.* **2016**, *2*, 1600495.
[30] F. S. Zhang, J. W. Wang, J. Luo, R. R. Liu, Z. M. Zhang, C. T. He, T. B. Lu, *Chem. Sci.* **2018**, *9*, 1375.
[31] Y. Pi, Q. Shao, X. Zhu, X. Huang, *ACS Nano* **2018**, *12*, 7371.
[32] J. Huang, H. Sheng, R. D. Ross, J. Han, X. Wang, B. Song, S. Jin, *Nat. Commun.* **2021**, *12*, 3036.
[33] M. Shamsuddin Ahmed, B. Choi, Y.-B. Kim, *Sci. Rep.*/ **2018**, *8*, 2543.
[34] R. Attias, K. Vijaya Sankar, K. Dhaka, W. Moschkowitsch, L. Elbaz, M. Caspary Toroker, Y. Tsur, *ChemSusChem* **2021**, *14*, 1737.
[35] A. Morozan, P. Jégou, B. Jousselme, S. Palacin, *Phys. Chem. Chem. Phys.* **2011**, *13*, 21600.
[36] T. Tachikawa, A. Beniya, K. Shigetoh, S. Higashi, *Catal. Lett.* **2020**, *150*, 1976.
[37] G. Lodi, E. Sivieri, A. de Battisti, S. Trasatti, *J. Appl. Electrochem.* **1978**, *8*, 135.
[38] R. L. Doyle, I. J. Godwin, M. P. Brandon, M. E. G. Lyons, *Phys. Chem. Chem. Phys.* **2013**, *15*, 13737.
[39] Y. Xu, F. Zhang, T. Sheng, T. Ye, D. Yi, Y. Yang, S. Liu, X. Wang, J. Yao, *J. Mater. Chem. A* **2019**, *7*, 23191.
[40] M. A. Bica De Moraes, B. C. Trasferetti, F. P. Rouxinol, R. Landers, S. F. Durrant, J. Scarmínio, A. Urbano, *Chem. Mater.* **2004**, *16*, 513.
[41] S. Blomberg, N. Johansson, E. Kokkonen, J. Rissler, L. Kollberg, C. Preger, S. M. Franzén, M. E. Messing, C. Hulteberg, *Materials* **2019**, *12*, 3727.
[42] J. R. Rumble, D. M. Bickham, C. J. Powell, *Surf. Interface Anal.* **1992**, *19*, 241.
[43] M. Casisi, S. Costanzo, P. Pinamonti, M. Reini, *Energies* **2019**, *12*, 114.
[44] M. C. Biesinger, B. P. Payne, L. W. M. Lau, A. Gerson, R. S. C. Smart, *Surf. Interface Anal.* **2009**, *41*, 324.
[45] M. C. Biesinger, B. P. Payne, A. P. Grosvenor, L. W. M. Lau, A. R. Gerson, R. S. C. Smart, *Appl. Surf. Sci.* **2011**, *257*, 2717.
[46] L. Yu, Q. Zhu, S. Song, B. McElhenny, D. Wang, C. Wu, Z. Qin, J. Bao, Y. Yu, S. Chen, Z. Ren, *Nat. Commun.* **2019**, *10*, 5106.
[47] P. K. Pandey, N. S. Bhave, R. B. Kharat, *Mater. Res. Bull.* **2006**, *41*, 1160.
[48] Y. Lykhach, S. Piccinin, T. Skála, M. Bertram, N. Tsud, O. Brummel, M. Farnesi Camellone, K. Beranová, A. Neitzel, S. Fabris, K. C. Prince, V. Matolín, J. Libuda, *J. Phys. Chem. Lett.* **2019**, *10*, 6129.
[49] L. Ma, S. Chen, H. Li, Z. Ruan, Z. Tang, Z. Liu, Z. Wang, Y. Huang, Z. Pei, J. A. Zapien, C. Zhi, *Energy Environ. Sci.* **2018**, *11*, 2521.
[50] Z. Xiao, Y. C. Huang, C. L. Dong, C. Xie, Z. Liu, S. Du, W. Chen, D. Yan, L. Tao, Z. Shu, G. Zhang, H. Duan, Y. Wang, Y. Zou, R. Chen, S. Wang, *J. Am. Chem. Soc.* **2020**, *142*, 12087.
[51] S. Xie, Y. Liu, J. Deng, J. Yang, X. Zhao, Z. Han, K. Zhang, H. Dai, *J. Catal.* **2017**, *352*, 282.
[52] K. Fan, H. Zou, Y. Lu, H. Chen, F. Li, J. Liu, L. Sun, L. Tong, M. F. Toney, M. Sui, J. Yu, *ACS Nano* **2018**, *12*, 12369.
[53] Y. Zhu, J. Wang, H. Chu, Y. C. Chu, H. M. Chen, *ACS Energy Lett.* **2020**, *5*, 1281.
[54] W. D. Chemelewski, H. C. Lee, J. F. Lin, A. J. Bard, C. B. Mullins, *J. Am. Chem. Soc.* **2014**, *136*, 2843.
[55] Z. Chen, L. Cai, X. Yang, C. Kronawitter, L. Guo, S. Shen, B. E. Koel, *ACS Catal.* **2018**, *8*, 1238.
[56] A. Bergmann, E. Martinez-Moreno, D. Teschner, P. Chernev, M. Gliech, J. F. de Araújo, T. Reier, H. Dau, P. Strasser, *Nat. Commun.* **2015**, *6*, 8625.
[57] K. M. Cole, D. W. Kirk, S. J. Thorpe, *J. Electrochem. Soc.* **2018**, *165*, J3122.
[58] B. S. Yeo, A. T. Bell, *J. Phys. Chem. C* **2012**, *116*, 8394.
[59] D. Song, L. Wang, M. Yao, W. Sun, R. Vajtai, P. M. Ajayan, Y. Wang, *Adv. Sustainable Syst.* **2020**, *4*, 2000227.
[60] B. S. Yeo, A. T. Bell, *J. Am. Chem. Soc.* **2011**, *133*, 5587.
[61] C. W. Tung, Y. Y. Hsu, Y. P. Shen, Y. Zheng, T. S. Chan, H. S. Sheu, Y. C. Cheng, H. M. Chen, *Nat. Commun.* **2015**, *6*, 8106.
[62] K. Rui, G. Zhao, Y. Chen, Y. Lin, Q. Zhou, J. Chen, J. Zhu, W. Sun, W. Huang, S. X. Dou, *Adv. Funct. Mater.* **2018**, *28*, 1801554.
[63] H. Y. Wang, Y. Y. Hsu, R. Chen, T. S. Chan, H. M. Chen, B. Liu, *Adv. Energy Mater.* **2015**, *5*, 1500091.
[64] T. W. Kim, M. A. Woo, M. Regis, K. S. Choi, *J. Phys. Chem. Lett.* **2014**, *5*, 2370.
[65] H. Y. Wang, S. F. Hung, H. Y. Chen, T. S. Chan, H. M. Chen, B. Liu, *J. Am. Chem. Soc.* **2016**, *138*, 36.
[66] H. Y. Wang, S. F. Hung, Y. Y. Hsu, L. Zhang, J. Miao, T. S. Chan, Q. Xiong, B. Liu, *J. Phys. Chem. Lett.* **2016**, *7*, 4847.
[67] Z. Yin, Y. Sun, C. Zhu, C. Li, X. Zhang, Y. Chen, *J. Mater. Chem. A* **2017**, *5*, 13648.